ACS Catalysis

pubs.acs.org/acscatalysis
Research Article

Acidic Oxygen Evolution Reaction Activity, Stability, and Durability of Copper and/or Manganese Cobalt Oxide Spinels

Christopher Pantayatiwong Liu, Ethan Hwjchim Vang, Tatiana Priamushko, Camille Roiron, Serhiy Cherevko, and Plamen Atanassov*

Cite This: ACS Catal. 2025, 15, 7956–7965
Read Online

ABSTRACT: Cu and Mn was incorporated into Co spinels and the structural and electrochemical properties of the resulting materials were investigated. Cu and Mn were found to reside exclusively in the octahedral sites in the spinel lattice. The incorporation of Mn and especially Cu improved initial activity for the oxygen evolution reaction in an acidic environment. The Mn-containing catalysts demonstrated substantially improved potential cycling durability. This was explained through cyclic voltammetry and online inductively coupled plasma mass spectrometry (ICP-MS) by the role of Mn on limiting the oxidation of tetrahedrally coordinated Co^{2+}. In potentiostatic conditions, however, pure Co spinel outperformed the multimetal oxides over time. In total, these findings stress the importance of stabilizing the tetrahedral Co^{2+} site through incorporation of other elements, and the improvements in electrochemical activity and stability that can thereby be realized.

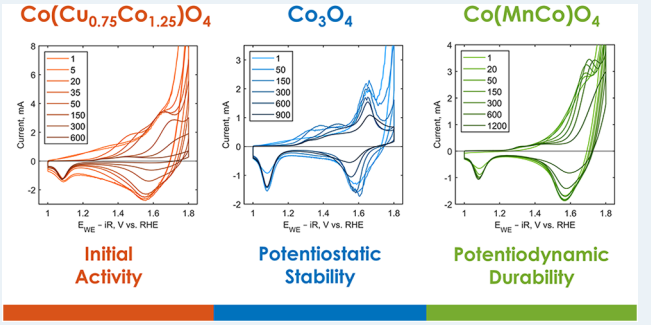

KEYWORDS: *acidic oxygen evolution reaction, metal oxide electrocatalysis, platinum-group-metal-free catalysis, catalyst durability in acidic OER, in situ ICP-MS, cobalt spinels*

INTRODUCTION

Renewably produced hydrogen from water electrolysis is poised to be an important technology for the clean energy transition, with governmental efforts around the world investing in its research, development, and deployment.[1] The oxygen evolution reaction (OER) is the bottleneck half-reaction in water electrolysis given its high overpotentials relative to the hydrogen evolution reaction and hence reducing the overpotential of the OER is important for advancing water electrolysis.

Although liquid alkaline water electrolyzers have a long industrial history, proton exchange membrane water electrolyzers (PEMWEs) are emerging as an alternative platform due to their ability to follow rapid changes in load and high power density (volumetric basis). Metal oxides represent the majority of OER catalysts[2,3] and while relatively stable in basic conditions, most metals, and their oxides, are thermodynamically unstable in acidic conditions.[4]

RuO_x, IrO_x, and mixtures of the two have long received substantial attention for catalyzing the OER in acid given their high activity and, for IrO_x-containing materials, stability.[5] These materials, however, are scarce and pose a technological risk when considering the needed gigawatt-scale deployment of water electrolysis for renewable hydrogen production.[6] Therefore, in conjunction with research on PEMWEs with low iridium loadings,[7] alternative, platinum-group-metal-free (PGM-free) catalysts for the OER in acid are increasingly being studied.[8,9]

Despite the harsh conditions of the OER in acid, several promising PGM-free catalysts for such conditions have been reported, e.g.,: γ-MnO_2,[10,11] $MnCo_2O_4$,[12] La- and Mn-codoped porous Co spinel fibers,[13] $Cu_{1.5}Mn_{1.5}O_4$:10F (doped with 10 wt % F),[14] Ag/Ti_nO_{2n-1},[15] and delaminated Co tungstate,[16] as well as a recent review on the topic.[17] Aside from Ag/Ti_nO_{2n-1} (Magneli phase), the catalysts mentioned have in common the presence of Cu, Mn, and/or Co as well as the spinel crystal phase. To explore this composition space, we built on previous work examining the activity of spinel $Co(CuCo)O_4$ for the OER in alkaline media[18] to contribute to what seems to be a promising family of catalysts. In total, four spinel-type catalysts—cobalt oxide, copper cobalt oxide, copper manganese cobalt oxide, and manganese cobalt oxide—were synthesized, characterized, and evaluated for activity, stability (potential hold), and durability (potential cycling) toward the OER at pH 1.

Received: January 22, 2025
Revised: April 16, 2025
Accepted: April 17, 2025
Published: April 29, 2025

METHODS

Synthesis. The catalysts were prepared following the sacrificial support method (SSM) with fumed silicas. In a typical synthesis, 1.4 g CAB-O-SIL LM-150 (150 m^2 g^{-1}, lot 4116657), 0.7 g Aerosil-90 (90 m^2 g^{-1}, lot 1010101100), and 0.7 g Aerosil-200 (200 m^2 g^{-1}, lot 1010101900) were combined with deionized water (18.2 MΩ, Milli-Q) and bath sonicated for 30 min. Depending on the desired catalyst composition, $Co(NO_3)_2{\cdot}6H_2O$ (98%, Sigma-Aldrich, lot BCBV8097), $Cu(NO_3)_2{\cdot}2.5H_2O$ (99.99%, Sigma-Aldrich, lot 11905CB), and/or $Mn(NO_3)_2{\cdot}6H_2O$ (97.0%, Sigma-Aldrich, lot BCBG6658 V) salts were added in stoichiometric molar ratios to the slurry, ensuring a salt to silica mass ratio of 0.75:1, and stirred for 30 min at room temperature. The slurry was dried overnight at 60 °C, ground using a mortar and pestle followed by 1 h of ball milling, and then calcinated in air at 250 °C for 12 h. Following this, the resulting black powder was then etched in 7 M KOH (Certified ACS grade, Fisher Chemical, lot 216832) overnight. Afterward, the powder was collected via centrifugation and vacuum filtration, followed by washing with copious amounts of deionized water. The powder was dried at 60 °C overnight, ground via mortar and pestle once more, and stored.

Structural Characterization. Powder X-ray diffraction (XRD) measurements were conducted on a Rigaku SmartLab X-ray diffractometer fitted with a monochromator (Cu Kα X-ray source, λ = 1.5405 Å, Ni foil Cu Kβ filter) with a zero-background Si sample holder. Secondary electron images were taken with both an FEI Magellan 400 XHR scanning electron microscope (SEM) as well as a JEOL JEM-2800 transmission electron microscope (TEM), and energy dispersive X-ray spectroscopy (EDS) maps were collected with the latter microscope. The elemental ratios were measured using inductively coupled plasma mass spectrometry (ICP-MS) with a Thermo Scientific iCAP RQ ICP-MS. Mn, Co, and Cu K edge X-ray absorption near edge spectroscopy (XANES) measurements were conducted on an easyXAFS300+. Spectra were normalized by the pre- and postedge regions and calibrated using Co, Cu, and Mn foils for the respective absorption edge. See Section 1 of the Supporting Information for more details.

Electrochemical Measurements. Electrochemical measurements were conducted with a three-electrode setup equipped with a Pine gold rotating disk electrode (RDE) tip as the working electrode, a graphite counter electrode in a fritted glass compartment, and a HydroFlex reference hydrogen electrode (RHE). 0.1 M $HClO_4$ (OmniTrace Ultra) was prepared with Milli-Q (IQ 7000) deionized water (18.2 MΩ). The RHE was measured to be within 3 mV of a platinum wire reference in H_2-saturated 0.1 M $HClO_4$. To ensure homogeneous films, the RDE tip was spray-coated. The exact catalyst loadings were assessed after deposition by measuring the change in mass of a heat-resistant poly(ethylene terephthalate) (PET) tape mask. For all the electrodes characterized, the catalyst loadings obtained were between 75 and 150 μg cm^{-2}. Inks were prepared with 1-propanol and Nafion D521 solution with a 1:21.5 catalyst to ionomer mass ratio and sonicated for at least 1 h in an iced water bath to minimize agglomeration. All measurements were conducted using a BioLogic VSP300 potentiostat and corrected on-the-fly for ohmic losses with an 85% compensation level, with the ohmic drop determined through electrochemical impedance spectroscopy. The rotation rate was set to 2500 rpm to assist with bubble removal.

Before activity, stability, and durability measurements were conducted, the working electrode was conditioned by sweeping from 1 V vs RHE to 1.8 V vs RHE at 100 mV s^{-1} 5 times. The activity for the OER was measured by taking the current at 1.65 V vs RHE during linear sweep voltammetry (LSV) measurements at a scan rate of 1 mV s^{-1}. Activity measurements were normalized both by the catalyst mass loading and the as-prepared catalyst surface area estimated from nitrogen adsorption isotherms using Brunauer−Emmett−Teller (BET) theory.

Stability measurements consisted of a 6 h potential hold at 1.75 V vs RHE. A 3 min potential hold at 1.6 V vs RHE was conducted before and after the 6 h hold to examine the effects on activity, and the change in current between the two 3 min holds was used as a metric of stability. Durability measurements were conducted by cycling between 1 V vs RHE and 1.8 V vs RHE at 500 mV s^{-1} with 5 s potential holds at each limit potential. In doing so, the durability test probes the ability of each catalyst to withstand surface oxidation and reduction, which translates to continuous contraction and relaxation of the lattice in the near-surface region.[19,20] Tests were concluded when the current at the end of a potential hold at 1.8 V vs RHE equaled 20% of the current at the end of the first cycle. We acknowledge the several studies highlighting that in RDE setups current loss due to O_2 coverage can be misinterpreted as catalyst degradation.[21,22] Based on current interrupt experiments as well as activity assessments before and after stability and durability tests, we confirm that adsorbed O_2 is not responsible for observed changes in activity (see section 5 of the Supporting Information, SI). All electrochemical experiments were repeated at least three times to ensure reproducibility.

Dissolution Measurements (Online ICP-MS). To prepare the catalyst inks for the dissolution measurements, the catalyst particles were dispersed in ultrapure water (Milli-Q IQ 7000 Merck) and 2-propanol (Emsure, Merck, ≥99.8% purity) mixture with a ratio of 7:1. Nafion (Sigma-Aldrich, 5 wt %) was added to the suspension as a binder to achieve 20 wt % of Nafion in the ink. The dispersions were sonicated with the sonication horn (Branson SFX 150) for around 20 min with intervals (4 s pulse, 2 s pause) and 40% intensity until the ink was homogeneous. The vial was kept on ice during sonication to prevent the heating of the ink and agglomeration of the particles. After sonication, the pH of the suspension was adjusted to ∼10 with 1 M KOH before drop-casting 0.25 μL of the suspension on a freshly polished glassy carbon (GC) plate (5 × 5 cm^2, Sigradur G, HTW), serving as a working electrode. The loading of the catalysts was aimed to be 20−22 μg cm^{-2}. The quality and the area of the drop-casted spots (average area of ca. 0.017 cm^2) were examined using the optical microscope (Keyence VK-X250).

The dissolution of the drop-casted samples was explored with a scanning flow cell (SFC) combined with ICP-MS, PerkinElmer Nexion 350X.[23] The working electrode was placed on a translational stage (Physik Instrumente M-403), allowing it to move along the electrode and quickly screen multiple samples. All electrochemical measurements were performed using a Gamry Reference 600 potentiostat. Homemade LabView software controlled all instruments (gas control box, mass flow controllers, peristaltic pump, and the translational stage). A glassy carbon rod and an Ag/AgCl

https://doi.org/10.1021/acscatal.5c00523
ACS Catal. 2025, 15, 7956−7965

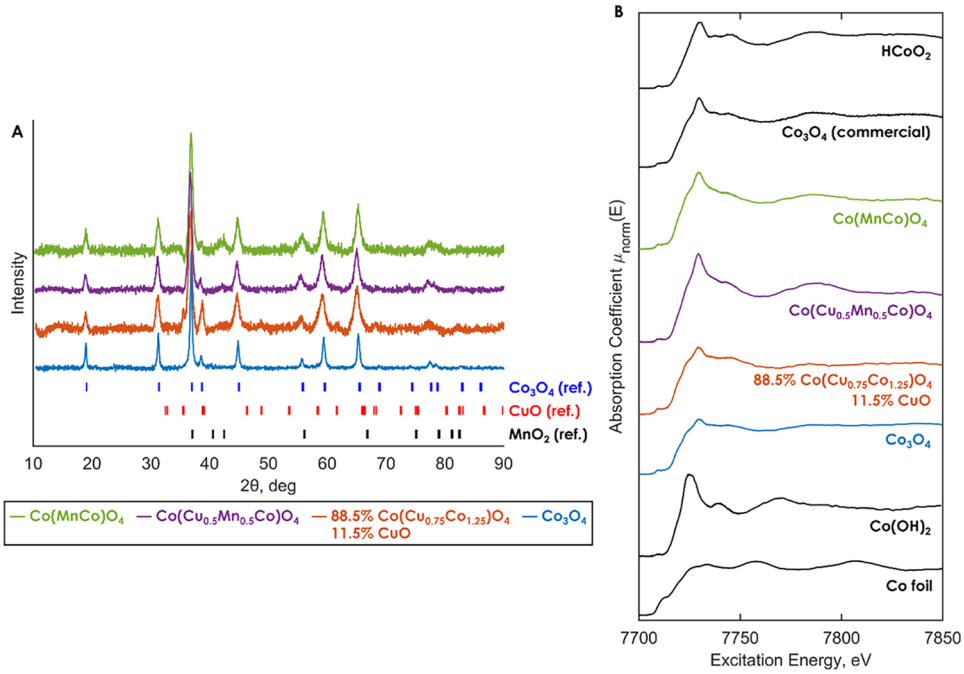

Figure 1. (A) Powder XRD spectra for, from top to bottom, $Co(MnCo)O_4$, $Co(Cu_{0.5}Mn_{0.5}Co)O_4$, $Co(Cu_{0.75}Co_{1.25})O_4$, Co_3O_4, $Co_{2.95}O_4$ (PDF 04−007−2519, $F\bar{4}_3m$), CuO (PDF 00−041−0254, $C2/c$), and MnO_2 (PDF 01−090−3404, $P6_3/mmc$). (B) Normalized Co K edge spectra of, from top to bottom, $HCoO_2$, commercial Co_3O_4, $Co(MnCo)O_4$ (green), $Co(Cu_{0.5}Mn_{0.5}Co)O_4$ (purple), $Co(Cu_{0.75}Co_{1.25})O_4$ (orange), and Co_3O_4 (blue), $Co(OH)_2$, and Co foil.

electrode (Metrohm) were used as counter and reference electrodes (CE and RE), respectively. Freshly prepared 0.05 M H_2SO_4 (96% Suprapur, Merck), saturated with Ar was used as an electrolyte and purged through the setup with a flow rate of 3.3 ± 0.1 $\mu L\ s^{-1}$. The electrolyte flow rate was controlled by the peristaltic pump of the ICP-MS (Elemental Scientific M2). The ICP-MS instrument was calibrated daily with known amounts of analyzed metals (^{55}Mn, ^{59}Co, and ^{63}Cu) and internal standard (^{74}Ge). To minimize the effect of polyatomic interferences, H_2SO_4 was used instead of $HClO_4$, and all the ICP-MS measurements were performed in a kinetic energy discrimination (KED) mode using He gas. To ensure the reproducibility of the results, all measurements were repeated at least twice on individual pristine drop-cast catalyst spots. Differences in surface areas were accounted for by normalizing the absolute currents with the geometric surface area of the catalyst spots.

RESULTS AND DISCUSSION

Structural Characterization. The XRD spectra of manganese cobalt oxide, copper manganese cobalt oxide, and cobalt oxide closely match that of spinel Co_3O_4 (PDF 04−007−2519, $F\bar{4}_3m$), as shown in Figure 1A. The lattice parameter was not significantly affected by the presence of the other metals. However, for copper cobalt oxide, there is an additional contribution from CuO (PDF 00−041−0254, $C2/c$); peak fitting yielded 11.6% CuO and 88.4% spinel (mass basis) for this material. The contribution of the CuO secondary phase to electrochemical measurements will be detailed in the following section.

From the metal molar ratios from ICP-MS analysis and the phase identification for each material, the composition of the spinels is as follows: Co_2MnO_4, $Co_2Cu_{0.5}Mn_{0.5}O_4$, and $Co_{2.25}Cu_{0.75}O_4$ and Co_3O_4. Previous studies on the structure of spinels suggest that the spinels incorporating Mn and Cu should crystallize in the inverse spinel structure, $B(AB)O_4$, as opposed to the normal spinel structure $A(B_2)O_4$, where the parentheses indicate metal atoms in octahedral sites and the position before representing atoms in tetrahedral sites.[24] The catalysts will here on be referred to following this assumption for the positions of metals and the composition of the spinel phases: $Co(MnCo)O_4$, $Co(Cu_{0.5}Mn_{0.5}Co)O_4$, $Co(Cu_{0.75}Co_{1.25})O_4$ and Co_3O_4, respectively (Table 1).

Table 1. Metal Molar Ratios from ICP-MS, BET Surface Areas, and Derived Chemical Formulas of the Synthesized Catalysts[a]

catalyst name	metal molar ratio from ICP-MS	BET surface area ($m^2\ g^{-1}$)
$Co(MnCo)O_4$	Mn: 1.05, Co: 1.95	95 ± 0.4
$Co(Cu_{0.5}Mn_{0.5}Co)O_4$	Cu: 0.47, Mn: 0.47, Co: 2.06	91 ± 0.4
$Co(Cu_{0.75}Co_{1.25})O_4$	Cu: 0.96, Co: 2.04	65 ± 2
Co_3O_4	N/A	35 ± 0.4

[a]Note that the Cu to Co molar ratio for copper cobalt oxide includes the Cu signal from the residual CuO.

To determine the placement of the Mn and Cu in the spinel lattice, Co K, Mn K, and Cu K edge spectra of the four catalysts were collected using an easyXAFS300+, along with additional reference materials for each absorption edge: Co foil, $Co(OH)_2$, Co_3O_4, CoOOH, Mn foil, Mn_2O_3, MnO_2, Cu foil, Cu_2O, and CuO. All spectra were normalized by linearly fitted pre- and postedge regions using the Larch analysis suite.[25] The normalized spectra of the Co K edge of the four catalysts along with the Co references are shown in Figure 1B. To understand the differences in Co oxidation state among the catalysts, we quantified the absorption edge energy shifts and

https://doi.org/10.1021/acscatal.5c00523
ACS Catal. 2025, 15, 7956−7965

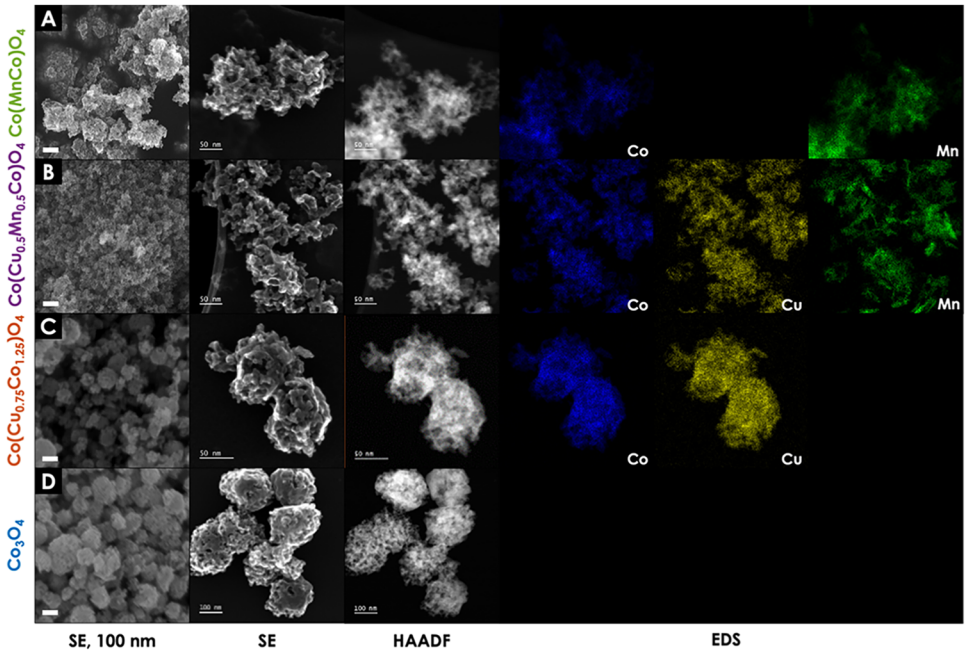

Figure 2. Rows: microscopy and spectroscopy of (A) $Co(MnCo)O_4$, (B) $Co(Cu_{0.5}Mn_{0.5}Co)O_4$, (C) $Co(Cu_{0.75}Co_{1.25})O_4$, and (D) Co_3O_4. Columns, from left to right: secondary electron (SE) images (SEM, through the lens detection mode), SE images (STEM), high angle annular dark field (HAADF) images, and mapped elemental distributions from EDS.

employed linear combination analysis using the spectra of reference oxides. For the shift quantification, two methods were used: (1) taking the average of the energies at 20, 50, and 80% of maximum absorption and (2) comparing the energies needed to reach a given integrated intensity.[26,27] The results of these analyses are shown in Figures S1−2 and Tables S1−3 in the Supporting Information. Ultimately, there was a uniform agreement in the trend that the oxidation state of Co increased as $Co(Cu_{0.75}Co_{1.25})O_4 \sim Co_3O_4 < Co(MnCo)O_4 < Co(Cu_{0.5}Mn_{0.5}Co)O_4$. There were large differences in the quantitative estimates of each catalyst's Co oxidation state between methods, however. The results of the linear combination analysis (Figure S3 and Table S4) using reference spectra of CoO (ID: h9xp85) and Co_3O_4 (ID: 9d44hc) from the XAS Database of the Canadian Light Source supported the Co oxidation state trend above.[28]

The Mn K absorption edge energy shifts of $Co(MnCo)O_4$ and $Co(Cu_{0.5}Mn_{0.5}Co)O_4$ showed that the oxidation state of Mn in both catalysts is closer to that of the Mn in MnO_2 than in Mn_2O_3 (Figure S4A and Table S5). Given that the tetrahedral site in cobalt spinels accommodates, in principle, up to a 2+ oxidation state cation, the Mn should then reside in the octahedral site where higher oxidation states are more tolerated. These results agree with other studies of manganese cobalt oxide spinels, which also concluded that Mn resides in the octahedral site.[12,13,29] The Cu K edge spectra of $Co(Cu_{0.75}Co_{1.25})O_4$ and $Co(Cu_{0.5}Mn_{0.5}Co)O_4$ are shown in Figure S4B, with the white line peak position of the two catalysts being nearly identical to that of CuO, suggesting similar coordination environments. The absorption edge shifts are tabulated in Table S6, revealing that the Cu in both $Co(Cu_{0.75}Co_{1.25})O_4$ and $Co(Cu_{0.5}Mn_{0.5}Co)O_4$ exist at a higher oxidation state than the Cu in CuO, which exists in a square planar coordination environment. Square planar coordination would be better accommodated at the octahedral sites in the cobalt spinel lattice, where the presence of the additional two ligands would explain the increased oxidation state of Cu in the spinels relative to CuO. The octahedral assignment is in agreement with other studies of copper cobalt oxide spinels.[30,31] From these results, we conclude that Mn and Cu are occupying the octahedral positions in the cobalt oxide spinels, and that the tetrahedral site is exclusively occupied by Co.

The BET surface areas of each catalyst are tabulated in Table 1. Despite using the same synthetic method for each catalyst, the Mn-containing catalysts showed higher BET specific surface areas. There are also qualitative differences in the morphologies of the catalysts visible in the SEM and STEM secondary electron images, (Figure 2). The high-angle annular dark-field (HAADF) images confirm the porous nature of the catalysts induced by the silica templates. EDS mappings of Co, Cu, and Mn of typical particles for the multimetal oxide catalysts confirm the homogeneous distribution of the metals.

Electrochemical Characterization. Initial activity at 1.65 V vs RHE increased in the order $Co_3O_4 < Co(Cu_{0.5}Mn_{0.5}Co)O_4 \sim Co(MnCo)O_4 < Co(Cu_{0.75}Co_{1.25})O_4$ when considering current normalized by either BET surface area or mass loading, as shown in Figure 3A,3B. The Au RDE tip negligibly contributes to the measured current (Figure S5). To explore the contribution of the minority CuO phase to the initial activity of $Co(Cu_{0.75}Co_{1.25})O_4$, we synthesized a separate batch of CuO, measured its initial activity, and concluded that it contributes less than 0.5% of the measured current in $Co(Cu_{0.75}Co_{1.25})O_4$ at 1.65 V vs RHE (Figure S6). In a study comparing $ZnCo_2O_4$, $CoAl_2O_4$, and Co_3O_4, the concentration activity increased as $ZnCo_2O_4 \ll CoAl_2O_4 \sim Co_3O_4$ which would suggest a link between the number of tetrahedrally coordinated Co^{2+} and OER activity in 0.1 M KOH.[32] For the present series of materials, however, the concentration of tetrahedrally coordinated Co^{2+} is the same and therefore cannot explain the differences in activity. Another study of a suite of CoMn spinels noted that activity

https://doi.org/10.1021/acscatal.5c00523
ACS Catal. 2025, 15, 7956−7965

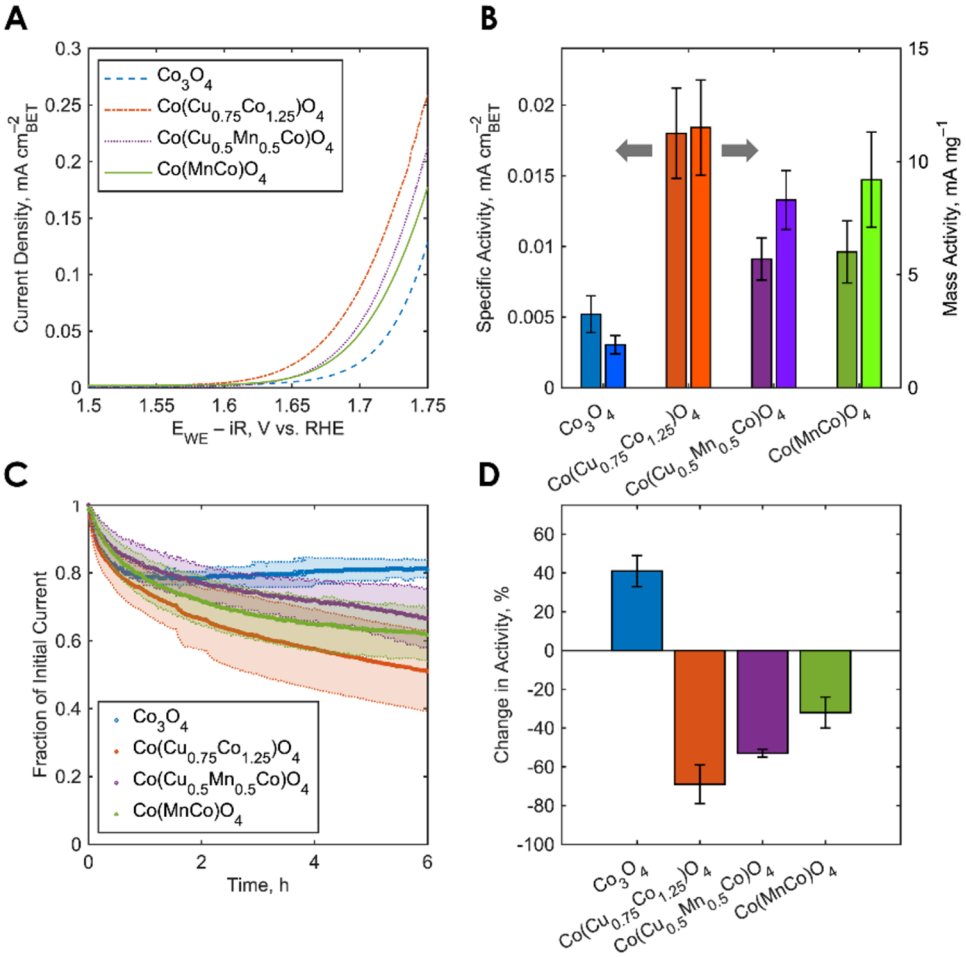

Figure 3. (A) Typical LSVs of each catalyst taken at a 1 mV s^{-1} scan rate. (B) OER activity measurements of the four catalysts normalized by BET surface area (left bars) and mass loading (right bars) taken from 1 mV s^{-1} LSVs at 1.65 V vs RHE. (C) CA results over the 6 h hold at 1.75 V vs RHE. (D) Change in OER activity after the 6 h at 1.75 V vs RHE from polarization curves taken before and after the hold (current taken at 1.6 V vs RHE).

in 0.05 M H_2SO_4 increased as the Co^{3+}:Co^{2+} increased.[33] In the current set of materials, $Co(Cu_{0.75}Co_{1.25})O_4$ exhibited both the lowest Co oxidation state and the highest initial activity, suggesting additional phenomena affecting the activity. For reference, we also note that $Co(Cu_{0.75}Co_{1.25})O_4$ exhibited a ca. 160 mV higher OER onset potential than that of commercial IrO_x (TANAKA Kikinzoku Kogyo K.K. 77110, Figure S7).

The current recorded during 6 h potential holds are plotted in Figure 3C. After a transient drop in current following the beginning of the hold due to bubble accumulation (Figures S8 and S9), the multimetal oxides exhibited a near linear current decay profile for the remainder of the test. Contrary to expectations, however, Co_3O_4 showed an increase in current approximately 2 h into the potential hold—the only material to do so. Comparison of polarization curves taken before and after the potential hold confirms this observation with Co_3O_4 showing an increase in activity following the potential hold (Figure 3D). Similar behavior and changes in activity were observed for Co_3O_4 after 15−24 h holds as well (Figure S10). The incorporation of Cu and Mn led to decreases in activity after the 6 h holds, with the effect being stronger for Cu. It is not clear, however, to what extent the current affected the stability results.

Typical CVs of each catalyst during the durability tests are shown in Figure 4A−D, as well as that of the bare Au RDE tip taken under the same conditions in Figure 4E. For all four catalysts, the Au RDE tip was responsible for the reductive peak at 1.1 V vs RHE and contributed no more than 0.35 mA with its oxidative peak at ca. 1.35 V vs RHE, its outline being easily distinguishable as the cycle numbers increase. For the catalysts, two oxidative peaks occurred at ca. 1.4 V vs RHE and 1.65 V vs RHE before the sharp rise in OER current which we ascribe to the Co^{2+}/Co^{3+} and Co^{3+}/Co^{4+} oxidative couples, respectively (denoted in Figure 4 as peaks 1 and 2, respectively).[32,34,35] The Co^{2+}/Co^{3+} oxidative peak was observed clearly for Co_3O_4 and $Co(Cu_{0.75}Co_{1.25})O_4$, where it quickly shifted to higher oxidative potentials with increased cycling, eventually becoming indistinguishable from the Co^{3+}/Co^{4+} oxidative peak. No feature corresponding to Co^{3+}/Co^{2+} reduction was observed, suggesting an irreversible oxidation of Co^{2+} for Co_3O_4 and $Co(Cu_{0.75}Co_{1.25})O_4$. The Co^{2+}/Co^{3+} oxidation peak for the Mn-containing catalysts was observed at higher potentials relative to Co_3O_4 and $Co(Cu_{0.75}Co_{1.25})O_4$. That said, the peak was barely resolvable, despite the Mn-containing catalysts having the same population of tetrahedrally coordinated Co^{2+} as Co_3O_4 and $Co(Cu_{0.75}Co_{1.25})O_4$ from the Mn K edge XANES results. This suggests that the presence of Mn hinders the oxidation of tetrahedrally coordinated Co^{2+}, which would allow for the presence of Co^{2+} tetrahedral sites through the OER potentials.

https://doi.org/10.1021/acscatal.5c00523
ACS Catal. 2025, 15, 7956−7965

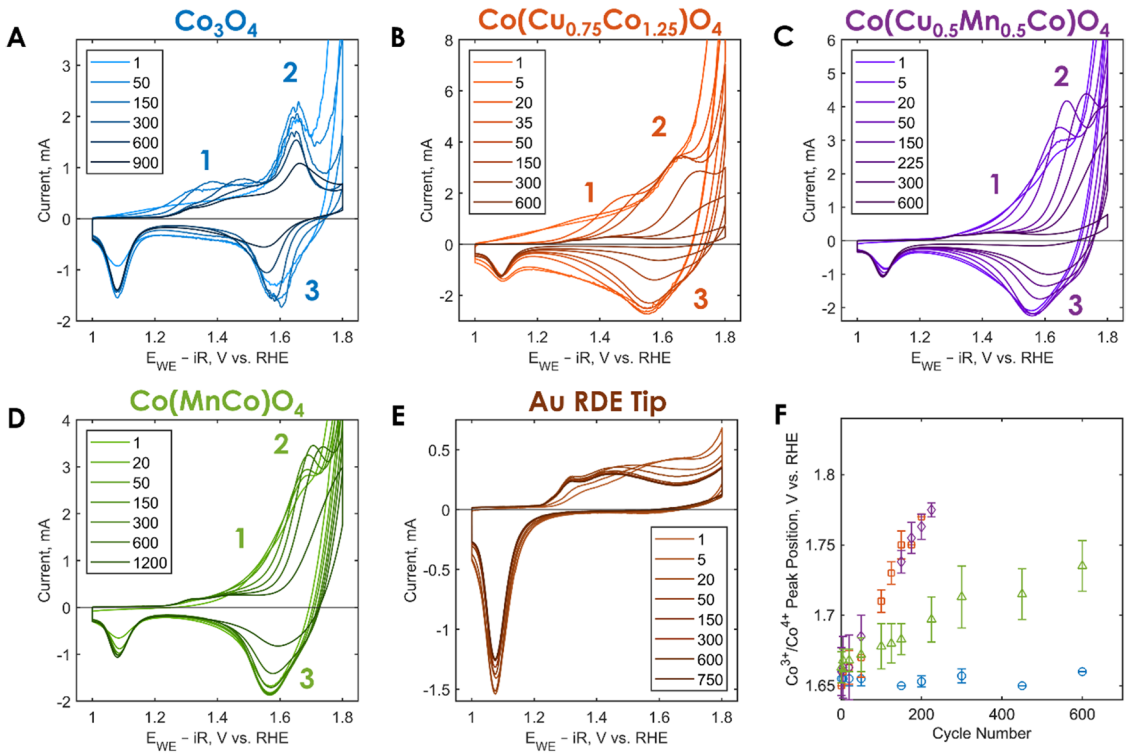

Figure 4. (A–D) Typical CVs of Co_3O_4, $Co(Cu_{0.75}Co_{1.25})O_4$, $Co(Cu_{0.5}Mn_{0.5}Co)O_4$, and $Co(MnCo)O_4$, respectively, during the durability tests (1–1.8 V vs RHE at 500 mV s^{-1} with 5 s holds at each limit potential in 0.1 M $HClO_4$, 85% ohmic compensation and 2500 rpm rotation rate). (E) CV of bare Au tip using the same durability protocol to measure maximum background current contribution. (F) Co^{3+}/Co^{4+} oxidative peak position versus number of cycles (blue circles: Co_3O_4, orange squares: $Co(Cu_{0.75}Co_{1.25})O_4$, purple diamonds: $Co(Cu_{0.5}Mn_{0.5}Co)O_4$, green triangles: $Co(MnCo)O_4$).

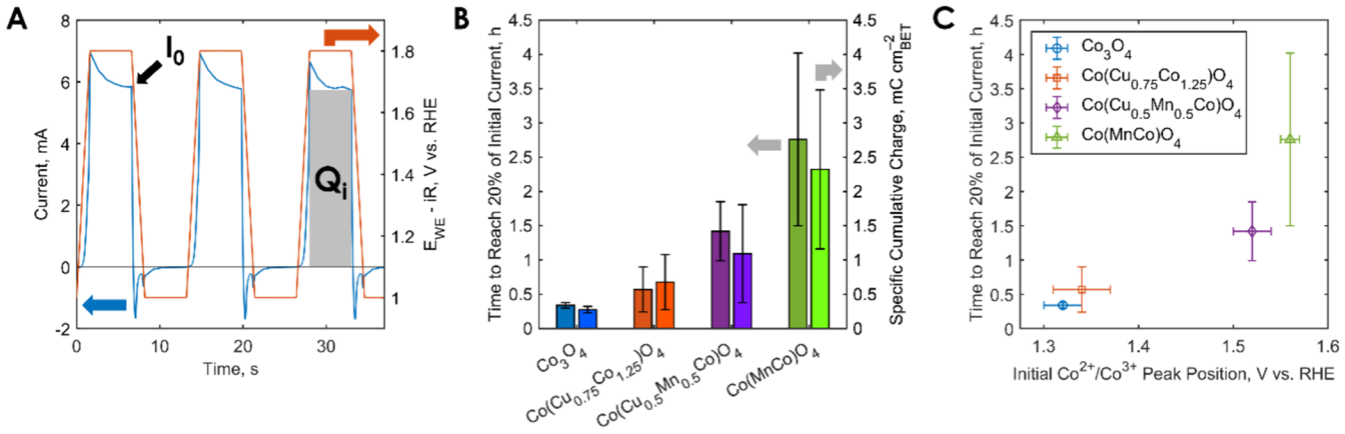

Figure 5. (A) First three cycles of Figure 4D with current plotted against time. The gray rectangle shows the assumed charged passed for the OER (Q_i) over each 5 s hold at 1.8 V vs RHE. (B) Left bars: time to reach 20% of initial current, I_0, during the potential cycling experiments. Right bars: cumulative charge passed at time when 20% of initial current is reached (calculated by summing Q_i). (C) Time to reach 20% of initial current versus the initial Co^{2+}/Co^{3+} oxidative peak position.

The reductive peak at ca. 1.6 V vs RHE is ascribed to Co^{4+}/Co^{3+} reduction (peak 3). For all the catalysts, the potential of the Co^{3+}/Co^{4+} oxidation peak was constant for the first cycles, and then shifted toward higher oxidative potentials. For Co_3O_4 and $Co(Cu_{0.75}Co_{1.25})O_4$, the Co^{3+}/Co^{4+} peak only began to shift once the potential of the Co^{2+}/Co^{3+} peak reached ca. 1.65 V vs RHE, suggesting a possible dependence. The potential shift of the Co^{3+}/Co^{4+} transition with the cycling is plotted for each catalyst in Figure 4F. The rate (i.e slope) of the shift increased in the following order: Co_3O_4 < $Co(MnCo)O_4$ < $Co(Cu_{0.5}Mn_{0.5}Co)O_4$ ~ $Co(Cu_{0.75}Co_{1.25})O_4$. We also acknowledge an alternative hypothesis for the redox peak assignments whereby in situ CoOOH oxidation and reduction may be occurring, which we plan on investigating in future work.

For each of the CVs, after sweeping from 1 V vs RHE to 1.8 V vs RHE, the potential was held for 5 s at 1.8 V vs RHE before the reverse sweep back to 1 V vs RHE. Current passed during this potential hold was assumed to be current from the OER with the final current reading taken as the representative OER current for that cycle. As represented in Figure 5A, the OER current for the first cycle is denoted as I_0, and the charge

https://doi.org/10.1021/acscatal.5c00523
ACS Catal. 2025, 15, 7956–7965

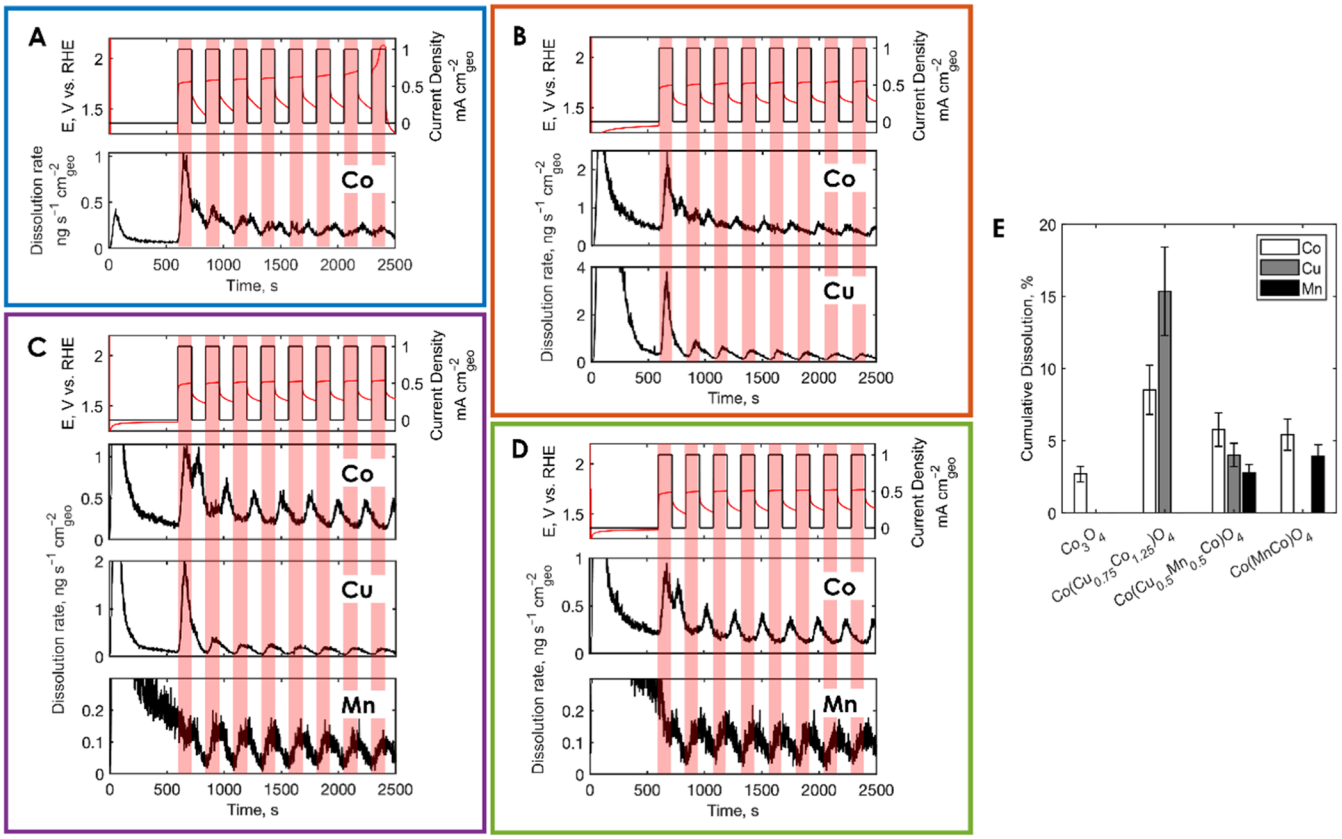

Figure 6. Typical metal dissolution rate measurements using a scanning flow cell coupled with online ICP-MS for (A) Co_3O_4, (B) $Co(Cu_{0.75}Co_{1.25})O_4$, (C) $Co(Cu_{0.5}Mn_{0.5}Co)O_4$, and (D) $Co(MnCo)O_4$ during open circuit and current pulsing conditions (potential in red, current in black). (E) Cumulative dissolution of Co, Cu, and Mn for each catalyst during the pulsing experiments.

passed for the OER for any given cycle denoted as Q_i, with i representing the cycle number. The time taken for the current to drop below 20% of the initial current, I_0, and the total OER charge passed during that time (specific cumulative charge) are plotted for each catalyst in Figure 5B. Potential cycling durability increased in the following order: Co_3O_4 < $Co(Cu_{0.75}Co_{1.25})O_4$ < $Co(Cu_{0.5}Mn_{0.5}Co)O_4$ < $Co(MnCo)O_4$. These results indicate that despite different initial activity trends (Figure 3B), the ability of the catalyst to withstand continuous oxidation and reduction determined the overall performance during the test. Lastly, the time to reach 20% of initial current was plotted versus the average initial Co^{2+}/Co^{3+} oxidative peak position for each catalyst in Figure 5C. This result suggests that trends in potential cycling durability for this class of materials could be indicated, or even predicted, by the difficulty of Co^{2+} oxidation measured through CV. We also note that this trend in Co^{2+}/Co^{3+} peak position is similar to the Co oxidation state trend extracted from the Co K XANES spectra.

Dissolution measurements of Co, Cu, and Mn from online ICP-MS with a current pulsing protocol are plotted below in Figure 6A–D. The y-axis was scaled to highlight the dissolution profiles during the pulsing regime (see Figure S11 for the full profiles). The current was pulsed between 0 and 1 mA cm^{-2} for 2 min each, several times, to study dissolution during the OER. Current control was chosen over potential control to ensure that all catalysts were catalyzing the OER during the measurement, with the understanding that less active catalysts (e.g., Co_3O_4) would experience higher potentials. Prominent Co dissolution was observed at contact, followed by dissolution that decayed with further cycling, corroborating the results of a previous study examining the transient behavior of Co_3O_4 in similar conditions.[35] For all catalysts but Co_3O_4, the Co dissolution rate was higher at open circuit than during pulsing at 1 mA cm^{-2}. For Co_3O_4, the Co dissolution peaks during pulsing (shaded in red) diminished with time and were noticeably absent by the seventh and eighth pulse cycles. Interestingly, this decrease in dissolution rate happens simultaneously with the increase in potential required to reach the pulse current. By the eighth cycle, the catalyst practically demonstrated failure. This behavior draws a parallel with the behavior of Co_3O_4 during the CV durability tests, where OER failure was reached approximately when the Co^{2+}/Co^{3+} oxidative peak shifted to that of the Co^{3+}/Co^{4+} peak, suggesting an exhaustion of Co^{2+}. This would suggest that the initial dissolution during the pulse is linked to the irreversible oxidation of Co^{2+}/Co^{3+}.

The Co dissolution peaks during operation subsided more quickly when Cu and especially Mn were incorporated into the catalyst. Also, the substantial loss in activity demonstrated by Co_3O_4 (rapid potential increase at the last 1 mA cm^{-2} pulse) was not observed for the multimetal catalysts. The dissolution profiles for Cu in both $Co(Cu_{0.75}Co_{1.25})O_4$ and $Co(Cu_{0.5}Mn_{0.5}Co)O_4$ presented a dissolution peak only when the current was switched from 0 to 1 mA cm^{-2}. This was also the case for Mn in $Co(Cu_{0.5}Mn_{0.5}Co)O_4$ and $Co(MnCo)O_4$ with a large dissolution peak surpassing that of Co during open circuit conditions. The large dissolution peaks observed during the first pulse cycle for Co and Cu were not observed for Mn. Co, Mn, and Cu dissolve when the potential is decreased,

https://doi.org/10.1021/acscatal.5c00523
ACS Catal. 2025, 15, 7956−7965

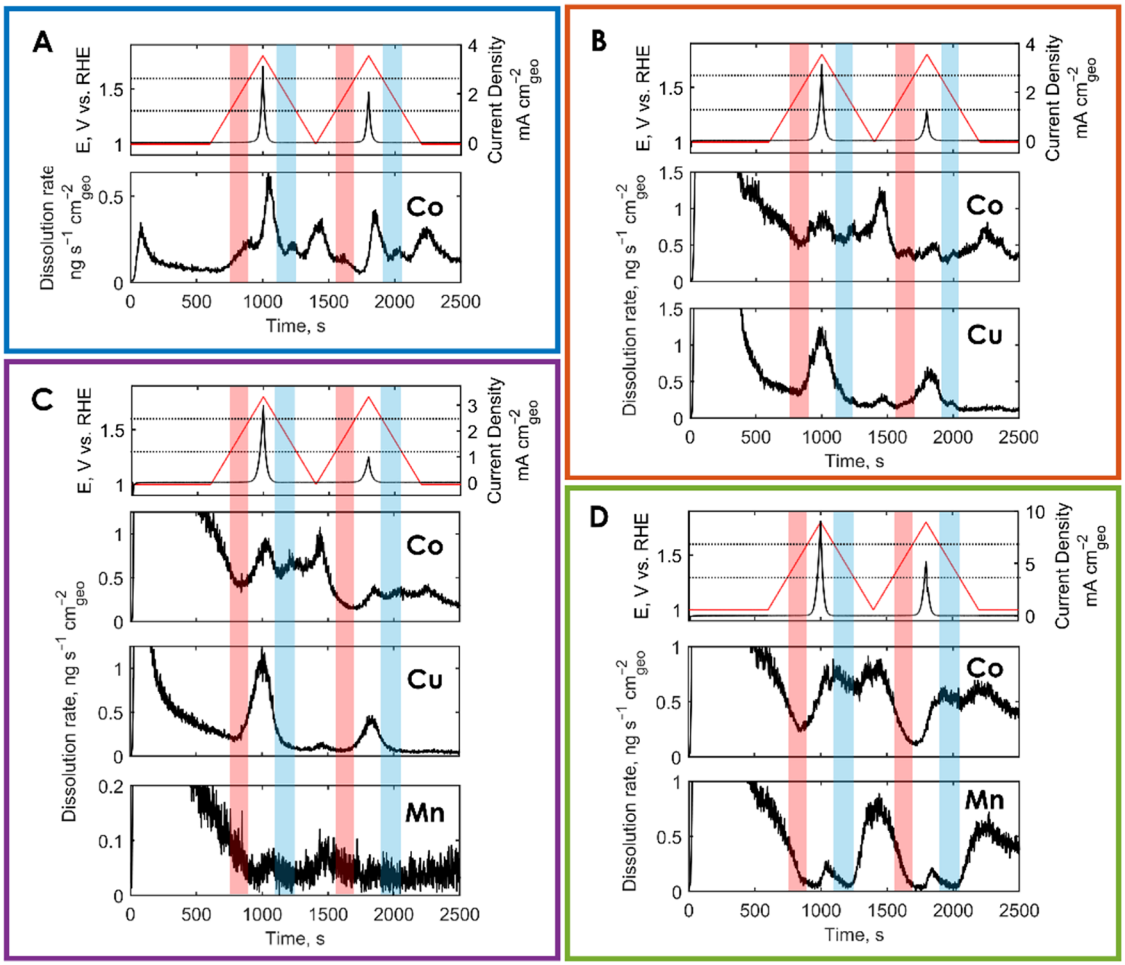

Figure 7. Typical metal dissolution rate measurements using a scanning flow cell coupled with online ICP-MS for (A) Co_3O_4, (B) $Co(Cu_{0.75}Co_{1.25})O_4$, (C) $Co(Cu_{0.5}Mn_{0.5}Co)O_4$, and (D) $Co(MnCo)O_4$ during a 1 V vs RHE hold followed by two CVs from 1 V vs RHE to 1.8 V vs RHE at 2 mV/s (potential in red, current in black). The red and blue shaded regions were added to highlight the dissolution profiles between 1.3 V vs RHE and 1.6 V vs RHE during the anodic and cathodic sweeps, respectively.

suggesting that the dissolution is likely induced by some reduction.

Figure 6E shows the cumulative dissolution of Co, Cu, and Mn for each catalyst, with total overall metal dissolution increasing in the order of Co_3O_4 < $Co(MnCo)O_4$ < $Co(Cu_{0.5}Mn_{0.5}Co)O_4$ < $Co(Cu_{0.75}Co_{1.25})O_4$. Co dissolution was less than 5% of the Co in Co_3O_4 during the pulsing test (Figure S12), with Co_3O_4 displaying the highest Co S-number (with $Co(MnCo)O_4$ closely approaching that of Co) (Figure S13). Despite Co_3O_4 displaying the lowest overall dissolution, it was the first catalyst to fail during both the pulsing experiments (Figure 6) and the CV durability tests (Figures 4 and 5). Therefore, total dissolution was not the primary factor governing the durability of the materials.

To study potential dependent dissolution, dissolution monitoring was also conducted during slow CVs taken from 1 V vs RHE to 1.8 V vs RHE, shown below in Figure 7. As in the pulsing experiments, the dissolution during the open circuit regime was higher for the multimetal oxides versus Co_3O_4. The dissolution profiles of Cu and/or Mn generally impose themselves on the dissolution profile of Co for each multimetal catalyst, suggesting that in some regions the dissolution of Co is accentuated by the dissolution of the other metals. The regions shaded in red and blue denote the potential window of Co^{2+}/Co^{3+} oxidation and, if reversible, Co^{3+}/Co^{2+} reduction, based on the results of Figure 4. In the red shaded regions, for Co_3O_4, the Co dissolution rate was increasing for the first CV and constant for the second (Figure 7A). For $Co(Cu_{0.75}Co_{1.25})O_4$, the Co dissolution rate decreased and then remained the same, respectively (Figure 7B). For the Mn-containing catalysts, however, Co dissolution decreased for both CVs within the same potential window (Figure 7C,D). Given that this potential window is where the assumed Co^{2+}/Co^{3+} oxidation reaction took place during the extended CV durability testing, these results can be interpreted as additional evidence of diminished Co^{2+}/Co^{3+} oxidative reactions for the Mn-containing compounds. The same trend was observed when stepping the potential from 1 V vs RHE to 1.4 V vs RHE, where the Co dissolution peak for Co_3O_4 in that window was not observed when Mn was introduced (Figure S14). As in Figure 7, Mn dissolution was only present during reductive events and low potentials, whereas Cu dissolution followed the opposite trend (Figure S14). For all the catalysts and most prominently for Co_3O_4, there was a Co dissolution peak that occurred slightly after OER current subsided—as it did not occur during OER, this suggests dissolution related to Co^{4+}/Co^{3+} reduction. In the blue shaded region, Co_3O_4 exhibited dissolution peaks for both cycles, whereas these peaks were less

https://doi.org/10.1021/acscatal.5c00523
ACS Catal. 2025, 15, 7956−7965

resolvable for the multimetal catalysts, decreasing in intensity as $Co(Cu_{0.75}Co_{1.25})O_4$ > $Co(Cu_{0.5}Mn_{0.5}Co)O_4$ > Co(MnCo)-O_4. From Figure 4, Co^{3+}/Co^{2+} reduction peaks were not easily observable for any of the catalysts, suggesting that the dissolution within the blue shaded region did not occur electrochemically.

Regarding the stability and durability of the catalysts, our results suggest that the irreversible oxidation and dissolution of tetrahedrally coordinated Co^{2+} is primarily responsible for the loss in activity over time for the materials studied. Despite Co_3O_4 exhibiting the lowest total dissolution during the current pulsing experiments, its activity decayed the most rapidly during both current pulsing and potential cycling experiments. This behavior was rationalized by the larger Co dissolution rates within the Co^{2+}/Co^{3+} redox potential window relative to the other catalysts. When Cu was added, durability improved slightly alongside less pronounced Co^{2+}/Co^{3+} oxidative current and lowered Co dissolution within the Co^{2+}/Co^{3+} redox potential window during both oxidative and reductive sweeps. This phenomenon was especially strong when Mn was introduced. Therefore, we conclude that the introduction of Mn diminishes Co^{2+}/Co^{3+} redox during transient operation and stabilizes the tetrahedrally coordinated Co^{2+}, which we hypothesize to be a key active site. This stabilizing effect was not demonstrated when the potential was instead held constant, suggesting that Co^{2+}/Co^{3+} irreversible oxidation is not triggered in that regime.

CONCLUSIONS

In sum, we observed that the incorporation of Cu in Co_3O_4 improved initial activity by approximately 3.5 times while the incorporation of Mn resulted in nearly an order of magnitude improvement in potential cycling durability. Given that the incorporation of Cu and especially Mn led to substantially improved potential cycling durability, we hypothesize that maintaining the integrity of tetrahedrally coordinated Co^{2+} in cobalt spinels is critical for maintaining activity over extended potential cycling operation. Improvements in stability versus Co_3O_4 during potentiostatic testing were not observed, however. As only Cu and Mn were incorporated in Co_3O_4 in this study, and in general the field of PGM-free acidic OER catalysts has explored a small set of elements, we see future opportunities to examine the incorporation of other elements in cobalt spinels and identify trends in activity and stability.

ASSOCIATED CONTENT

Supporting Information

The Supporting Information is available free of charge at https://pubs.acs.org/doi/10.1021/acscatal.5c00523.

Additional details on the XANES, electrochemistry, and in situ ICP-MS methods and measurements (PDF).

AUTHOR INFORMATION

Corresponding Author

Plamen Atanassov − *Department of Chemical and Biomolecular Engineering, University of California, Irvine, California 92697, United States;* orcid.org/0000-0003-2996-472X; Email: plamen.atanassov@uci.edu

Authors

Christopher Pantayatiwong Liu − *Department of Chemical and Biomolecular Engineering, University of California, Irvine, California 92697, United States;* orcid.org/0000-0002-1064-2133

Ethan Hwjchim Vang − *Department of Chemical and Biomolecular Engineering, University of California, Irvine, California 92697, United States*

Tatiana Priamushko − *Helmholtz-Institute Erlangen-Nürnberg for Renewable Energy (IET-2), Forschungszentrum Jülich, Erlangen 52428, Germany;* orcid.org/0000-0002-1511-7784

Camille Roiron − *Department of Chemical and Biomolecular Engineering, University of California, Irvine, California 92697, United States;* orcid.org/0000-0001-9772-8249

Serhiy Cherevko − *Helmholtz-Institute Erlangen-Nürnberg for Renewable Energy (IET-2), Forschungszentrum Jülich, Erlangen 52428, Germany;* orcid.org/0000-0002-7188-4857

Complete contact information is available at: https://pubs.acs.org/10.1021/acscatal.5c00523

Notes

The authors declare no competing financial interest.

ACKNOWLEDGMENTS

C.P.L. thanks Dr. Philippe Allongue, Dr. Yu Morimoto, Dr. Arno Bergmann, and Dr. Marian Chatanet for the insightful discussions on the electrochemical measurements. C.P.L. acknowledges support from the National Science Foundation Graduate Research Fellowship under Grant No. DGE-1839285. T.P. acknowledges support from the Alexander von Humbolt Foundation. The authors acknowledge the use of facilities and instrumentation at the UC Irvine Materials Research Institute (IMRI), which is supported in part by the National Science Foundation through the UC Irvine Materials Research Science and Engineering Center (DMR-2011967).

REFERENCES

(1) IEA. *The Future of Hydrogen*, International Energy Agency2019.

(2) Fabbri, E.; Habereder, A.; Waltar, K.; Kötz, R.; Schmidt, T. J. Developments and perspectives of oxide-based catalysts for the oxygen evolution reaction. *Catal. Sci. Technol.* **2014**, *4* (11), 3800−3821.

(3) Suen, N. T.; Hung, S. F.; Quan, Q.; Zhang, N.; Xu, Y. J.; Chen, H. M. Electrocatalysis for the oxygen evolution reaction: Recent development and future perspectives. *Chem. Soc. Rev.* **2017**, *46* (2), 337−365.

(4) Pourbaix, M. *Atlas of Electrochemical Equilibria in Aqueous Solutions*; National Association of Corrosion Engineers: Houston, 1974.

(5) Trasatti, S. Electrocatalysis in the Anodic Evolution of Oxygen in Chlorine. *Electrochim. Acta* **1984**, *29* (11), 1503−1512.

(6) Clapp, M.; Zalitis, C. M.; Ryan, M. Perspectives on current and future iridium demand and iridium oxide catalysts for PEM water electrolysis. *Catal. Today* **2023**, *420*, No. 114140, DOI: 10.1016/j.cattod.2023.114140.

(7) Wang, C.; Lee, K.; Liu, C. P.; et al. Design of PEM water electrolysers with low iridium loading. *Int. Mater. Rev.* **2024**, *69* (1), 3−18.

(8) Liu, L. Platinum group metal free nano-catalysts for proton exchange membrane water electrolysis. *Curr. Opin. Chem. Eng.* **2021**, *34*, No. 100743, DOI: 10.1016/j.coche.2021.100743.

(9) Cherevko, S. Stabilization of Non-Noble Metal Electrocatalysts for Acidic Oxygen Evolution Reaction. *Curr. Opin. Electrochem.* **2023**, *38*, No. 101213.

(10) Li, A.; Ooka, H.; Bonnet, N.; et al. Stable Potential Windows for Long-Term Electrocatalysis by Manganese Oxides Under Acidic Conditions. *Angew. Chem., Int. Ed.* **2019**, *58* (15), 5054−5058.
(11) Kong, S.; Li, A.; Long, J.; et al. Acid-stable manganese oxides for proton exchange membrane water electrolysis. *Nat. Catal.* **2024**, *7* (3), 252−261.
(12) Li, A.; Kong, S.; Guo, C.; et al. Enhancing the stability of cobalt spinel oxide towards sustainable oxygen evolution in acid. *Nat. Catal.* **2022**, *5* (2), 109−118.
(13) Chong, L.; Gao, G.; Wen, J.; et al. La-and Mn-doped cobalt spinel oxygen evolution catalyst for proton exchange membrane electrolysis. *Science* **2023**, *380*, 609−616.
(14) Patel, P. P.; Datta, M. K.; Velikokhatnyi, O. I.; et al. Noble metal-free bifunctional oxygen evolution and oxygen reduction acidic media electro-catalysts. *Sci. Rep.* **2016**, *6*, No. 28367, DOI: 10.1038/srep28367.
(15) Siracusano, S.; Giacobello, F.; Aricò, A. S. Ag/Ti-suboxides as non-PGM anode electrocatalyst for PEM water electrolysis. *J. Power Sources* **2023**, *565*, No. 232903, DOI: 10.1016/j.jpowsour.2023.232903.
(16) Ram, R.; Xia, L.; Benzidi, H.; et al. Water-hydroxide trapping in cobalt tungstate for proton exchange membrane water electrolysis. *Science* **2024**, *384* (6702), 1373−1380.
(17) Liu, T.; Chen, C.; Pu, Z.; et al. Non-Noble-Metal-Based Electrocatalysts for Acidic Oxygen Evolution Reaction: Recent Progress, Challenges, and Perspectives. *Small* **2024**, *20*, No. 2405399, DOI: 10.1002/smll.202405399.
(18) Serov, A.; Andersen, N. I.; Roy, A. J.; Matanovic, I.; Artyushkova, K.; Atanassov, P. CuCo 2 O 4 ORR/OER Bi-Functional Catalyst: Influence of Synthetic Approach on Performance. *J. Electrochem. Soc.* **2015**, *162* (4), F449−F454.
(19) Bouvier, M.; Bubi, I. P.; Wiegmann, T.; et al. Unraveling the Cobalt Oxidation State at the Surface of Epitaxial Cobalt Oxide Films during the Oxygen Evolution Reaction by Operando X-ray Absorption Spectroscopy/Surface X-ray Diffraction. *ACS Appl. Energy Mater.* **2023**, *6* (14), 7335−7345.
(20) Reikowski, F.; Maroun, F.; Pacheco, I.; et al. Operando Surface X-ray Diffraction Studies of Structurally Defined Co3O4 and CoOOH Thin Films during Oxygen Evolution. *ACS Catal.* **2019**, *9* (5), 3811−3821.
(21) El-Sayed, H. A.; Weiß, A.; Olbrich, L. F.; Putro, G. P.; Gasteiger, H. A. OER Catalyst Stability Investigation Using RDE Technique: A Stability Measure or an Artifact? *J. Electrochem. Soc.* **2019**, *166* (8), F458−F464.
(22) Hartig-Weiss, A.; Tovini, M. F.; Gasteiger, H. A.; El-Sayed, H. A. OER catalyst durability tests using the rotating disk electrode technique: The reason why this leads to erroneous conclusions. *ACS Appl. Energy Mater.* **2020**, *3* (11), 10323−10327.
(23) Kasian, O.; Geiger, S.; Mayrhofer, K. J. J.; Cherevko, S. Electrochemical on-line ICP-MS in electrocatalysis research. *Chem. Rec.* **2019**, *19* (10), 2130−2142.
(24) Burdett, J. K.; Price, G. D.; Price, S. L. Role of the Crystal-Field Theory in Determining the Structures of Spinels. *J. Am. Chem. Soc.* **1982**, *104*, 92−95.
(25) Newville, M. Larch: An Analysis Package for XAFS and Related Spectroscopies. *J. Phys.:Conf. Ser.* **2013**, *430*, No. 012007.
(26) Henderson, G. S.; De Groot, F. M. F.; Moulton, B. J. A. X-ray Absorption Near-Edge Structure (XANES) Spectroscopy. *Rev. Mineral. Geochem.* **2014**, *78* (1), 75−138.
(27) Capehart, T. W.; Herbst, J. F.; Mishra, R. K.; Pinkerton, F. E. X-ray-absorption edge shifts in rare-earth−transition-metal compounds. *Phys. Rev. B* **1995**, *52* (11), No. 7907.
(28) Canadian Light Source. XAS Database (XASDB) 2025 http://xasdb.lightsource.ca.
(29) Wang, W.; Kuai, L.; Cao, W.; et al. Mass-Production of Mesoporous MnCo2 O4 Spinels with Manganese(IV)- and Cobalt-(II)-Rich Surfaces for Superior Bifunctional Oxygen Electrocatalysis. *Angew. Chem.* **2017**, *129* (47), 15173−15177.
(30) Li, G.-H.; Dai, L.-Z.; Lu, D.-S.; Peng, S.-Y. Characterization of Copper Cobalt Mixed Oxide. *J. Solid State Chem.* **1990**, *89*, 167−173.
(31) La Rosa-Toro, A.; Berenguer, R.; Quijada, C.; Montilla, F.; Morallón, E.; Vázquez, J. L. Preparation and characterization of copper-doped cobalt oxide electrodes. *J. Phys. Chem. B* **2006**, *110* (47), 24021−24029.
(32) Wang, H. Y.; Hung, S. F.; Chen, H. Y.; Chan, T. S.; Chen, H. M.; Liu, B. In Operando Identification of Geometrical-Site-Dependent Water Oxidation Activity of Spinel Co3O4. *J. Am. Chem. Soc.* **2016**, *138* (1), 36−39.
(33) Huang, J.; Borca, C. N.; Huthwelker, T.; et al. Surface oxidation/spin state determines oxygen evolution reaction activity of cobalt-based catalysts in acidic environment. *Nat. Commun.* **2024**, *15* (1), No. 3067.
(34) Natarajan, K.; Munirathinam, E.; Yang, T. C. K. Operando Investigation of Structural and Chemical Origin of Co3O4Stability in Acid under Oxygen Evolution Reaction. *ACS Appl. Mater. Interfaces* **2021**, *13* (23), 27140−27148.
(35) Priamushko, T.; Franz, E.; Logar, A.; et al. Be Aware of Transient Dissolution Processes in Co3 O4 Acidic Oxygen Evolution Reaction Electrocatalysts. *J. Am. Chem. Soc.* **2025**, *147*, 3517−3528.

https://doi.org/10.1021/acscatal.5c00523
ACS Catal. 2025, 15, 7956−7965